Radio Science

RESEARCH ARTICLE
10.1029/2022RS007500

Manx Arrays: Perfect Non-Redundant Interferometric Geometries

D. McKay[1,2], T. Grydeland[3], and B. Gustavsson[4]

[1]Finnish Centre for Astronomy with ESO (FINCA), University of Turku, Turku, Finland, [2]Aalto University Metsähovi Radio Observatory, Kylmälä, Finland, [3]NORCE Norwegian Research Center AS, Tromsø, Norway, [4]UiT—The Arctic University of Norway, Langnes, Norway

Key Points:

- A "perfect array" is a mathematical construct with uniform and complete element spacings to a circle of radius up to the maximum uv-distance
- The Manx array represents the configuration of the largest perfect array
- Fractal replication of the Manx array results in *uv*-efficient layouts

Correspondence to:

D. McKay,
derek.mckay@utu.fi

Citation:

McKay, D., Grydeland, T., & Gustavsson, B. (2022). Manx arrays: Perfect non-redundant interferometric geometries. *Radio Science*, *57*, e2022RS007500. https://doi.org/10.1029/2022RS007500

Received 6 MAY 2022
Accepted 31 AUG 2022

Author Contributions:

Conceptualization: B. Gustavsson
Formal analysis: T. Grydeland, B. Gustavsson
Methodology: T. Grydeland, B. Gustavsson
Supervision: T. Grydeland, B. Gustavsson
Validation: D. McKay
Visualization: D. McKay, T. Grydeland, B. Gustavsson
Writing – original draft: D. McKay
Writing – review & editing: D. McKay, T. Grydeland, B. Gustavsson

Abstract Interferometry applications (e.g., radio astronomy) often wish to optimize the placement of the interferometric elements. One such optimal criterion is a uniform distribution of non-redundant element spacings (in both distance and position angle). While large systems, with many elements, can rely on saturating the sample space, and disregard "wasted" sampling, small arrays with only a few elements are more critical, where a single element can represent a significant fraction of the overall cost. This paper defines a "perfect array" as a mathematical construct having uniform and complete element spacings within a circle of radius equal to the maximum element spacing. Additionally, the largest perfect non-redundant array, comprising six elements, is presented. The geometry is described, along with the properties of the layout and situations where it would be of significant benefit to array application and non-redundant masking designs.

Plain Language Summary An interferometer combines an array of separate elements (e.g., radio antennas or optical apertures) to receive electromagnetic waves. The position of these elements relative to each other will affect the quality of the resultant combined measurement. This paper defines a "perfect non-redundant" array as one where the different relative positions have been chosen to give the best possible result, without any unnecessary duplication. This optimization improves the efficiency, and reduces the size and cost, of such an interferometer design. This paper reports on the largest such array—the Manx array.

1. Introduction

In radio astronomy and other applications where radio interferometry is employed, it is common to want to select the placement of antennas (interferometric array elements) to obtain some form of optimal response function.

The general use of interferometry in a radio astronomy context can be explored in (e.g., Thompson et al., 2017). In such an interferometer, the correlation of the signal (measured E-field) incident at each pair of antennas is determined. The length and orientation of the vector between two antennas, projected onto the plane perpendicular to the line of sight (referred to as the *uv*-plane), determines the instrument's spatial sensitivity and thus antenna locations are often selected in an attempt to optimize the desired response (Taylor et al., 1999). What constitutes "optimal" is subjective and depends on the application; a scientific-versus a technical-perspective may assess this differently. And it is also acknowledged that pragmatism is required in many real-world applications to deal with external factors (such as geography, connectivity, or cost).

However, one common optimization goal is that of removing redundancy (duplicate or near-duplicate sampling of positions in the *uv*-plane. An early case for this was made by (Greenaway, 1979) aiming for observing efficiency. From the perspective of imaging, benefits of uniform *uv*-sampling for sparse arrays are stated by (Keto, 1997). In comparison (Boone, 2002), analyzed dense arrays and concluded that Gaussian radial-distributions achieve a desired Gaussian beam. Numerous attempts at optimization of antenna placement have been reported (e.g., Boone, 2001; Cohanim et al., 2004; Cornwell, 1988; Gauci et al., 2013; Kogan, 2000; Kiehbadroudinezhad et al., 2017; Su et al., 2004). Consideration has also been given to how add to an existing array optimally (e.g., Karastergiou et al., 2006).

This paper treats optimal as the geometric objective of obtaining an instantaneous, uniform-distribution of sampling of the Fourier domain. As the number of antennas in the interferometer is discrete, then the interferometric sampling of the Fourier domain is also discrete. This means that while the sampling may be uniform, it is not continuous. The sampling in the Fourier domain is uniform (in distribution); there is no one sample closer to

another in the Fourier domain. This signifies "non-redundant" optimization. The uniform sampling extends to a radius in the Fourier domain equivalent to the largest baseline. There are no irregularities in the distribution of Fourier sampling, which signifies the mathematically "perfect" geometry. In this context, a perfect array is this a regular distribution of *uv*-spacings within a circle of radius equal to the maximum *uv*-distance.

In this paper, a particular arrangement of six elements is considered. The configuration is referred to it as a **Manx array**, owing to the similarity between the layout and the triskelion that appears on the *brattagh Vannin* (the flag of the Isle of Man). This array can be considered as the largest perfect non-redundant interferometric geometry, in that its difference vectors between elements (the so-called baselines) have uniform distribution, resulting in uniform instantaneous sampling of the Fourier domain (also known as uniform *uv*-coverage). The number of antennas is small, which makes this study distinct from the aforementioned studies which consider large numbers and statistical distributions.

The additional property is that there are no "redundant" spacings. Redundant spacings contribute to additional sampling of the *same* Fourier components, which leads to increased sensitivity and noise-reduction, and there may be other motivations for including them in an array (such as calibration and signal-integrity validation). Experimental motivations exist for deliberately including redundancy in an array (e.g., the Westerbork Synthesis Radio Telescope [Hogbom & Brouw, 1974]). However the redundancy does not contribute spatial information.

2. Development

From 2006 to 2009, the EISCAT Scientific Association carried out a design study for a new incoherent scatter radar (van Eyken et al., 2009). The previous EISCAT radar comprised mechanically steered parabolic dish antennas. However, the new facility (named EISCAT_3D) would comprise phased-array antenna systems. As part of that study, consideration was given to the use of interferometry and optimal array layouts (good coverage of the *uv*-plane, with few redundant baselines) were sought. This led to the report of a 7-element configuration (Grydeland & La Hoz, 2006, figure 6). It was subsequently discovered that omission of the central element of this configuration, and bringing the remaining elements closer to the center, resulted in an array with a hexagonally packed *uv*-spacing with no redundant baselines. Although studies of small-number arrays from different disciplines (radio astronomical [Cornwell, 1988] and geometric set theory [Blackburn, Etzion, et al., 2010]) have been carried out, none have noted this configuration. Subsequent work focused on complementing Costas-arrays (Costas, 1984; Golomb & Taylor, 1984) with additional elements producing difference vector sets with more complete *uv*-coverage. Of particular interest were the 2×2, 3×3 and one of the 4×4 Costas arrays, that were possible to complement such that a perfect distribution of difference vectors can be achieved. However, for Costas arrays larger than 4×4 no perfect filling has been found. This search-method is less constrained than the cyclid-different-set-based approach used by, for example, Kopilovich (1998), however the perfect difference-vector set requirement used here is stricter.

Non-redundant arrays have numerous uses in radio applications, but are also relevant in other fields; for example, optical interferometric masks (Greenbaum et al., 2014; Sallum & Skemer, 2019). Examination of the observing efficiency of arrays of discrete element interferometers demonstrates that configurations in which the elements are spaced non-redundantly, gives the most efficient array (Greenaway, 1979, e.g.,).

Methods have been attempted to find ideal configurations (Kogan, 2000), and this has also been done for EISCAT-related projects. For example, for the EASI study (Grydeland et al., 2005), random configurations were chosen and tested, with the performance metrics being the FWHM of the primary lobe (the zeroth antinode) and the minimum height of any sidelobe response outside of the first null. Here, sidelobe refers to a local maximum response between the zeroth and first antinodes. The same principle, as used in the EASI study, was applied when adding two additional antennas to the KAIRA array (McKay-Bukowski et al., 2015).

In addition to mass-sampling of random configurations, optimization techniques have been applied to the problem. These methods either aim to minimize the sidelobe levels of the synthesized beam, for example, by the so-called "push-pull" algorithm (Huang et al., 2019), or the *uv*-distribution by "sieving" (Su et al., 2004), or adjusting *uv*-distributions toward a desired target distribution by tomographic methods (De Villiers, 2007). Such techniques can be used to optimize array configurations for snap-shot or for longer-duration observations (e.g., Boone, 2001). These also result in a well-distributed set of *uv*-spacings, and result in low-sidelobe characteristics of the synthetic beam.

3. Consideration of Layout

Mathematically, the Manx array coordinates can be created by taking two unit vectors, $\vec{e}_1$ and $\vec{e}_2$, defined as:

$$\left.\begin{aligned}\vec{e}_1 &= [1, 0] \\ \vec{e}_2 &= [\cos(\pi/3), \sin(\pi/3)]\end{aligned}\right\} \quad (1)$$

Note that e_2 is the equivalent of the e_1 unit vector rotated counter-clockwise by 60°. The Manx array is then formed from applying the coordinate set, m:

$$m = \{[0, 0], [1, 0], [2, 1], [1, 2], [-1, 2], [-1, 3]\} \quad (2)$$

in the directions of $\vec{e}_1$ and $\vec{e}_2$.

The beam forming properties of the array are related to the baselines (spacings, in both distance and position angle) between the elements. The number of baselines, B, is related to the number of antennas, N, by the expression $B = N(N - 1)/2$. Although more antennas means more baselines, these baselines may not necessarily be unique. For example, 3 antennas, equispaced on a line will have three baselines. However, the baseline from element 1 to element 2 will be exactly the same as the baseline from element 2 to element 3. These baselines are redundant, in that they sample the same point in the Fourier domain. Additional antennas do add to the sensitivity of the array, however there is no improvement to the beam response function (in terms of beam shape).

Array designers, particularly in radio astronomy, have sought to find array layouts which avoid these redundant—or near-redundant—baselines. Even more difficult is finding array configurations where the baselines are uniformly distributed, thus representing a regular sampling of the Fourier domain. This Fourier parameter space is typically plotted on a graph referred to as a *uv*-diagram (the differential spatial axes are u and v) and the distribution of sampling in this domain is referred to as *uv*-coverage. Evenly sampled, non-redundant arrays are referred to as perfect arrays. Here "evenly sampled" means that all baselines smaller than or equal to the diameter of the array must be present on the triangular grid.

The progression of perfect arrays applies for 1, 2, 3, 4 and six elements. The 1-element case is degenerate and the 2-element case is trivial and non-confined. The remainder are shown in Figure 1. The bottom two panels show the Manx array layout (lower left) and the resultant *uv*-coverage (lower right). Perfect arrays possess rotational symmetry and the Manx array has a chiral opposite (not shown). For larger arrays, there are no configurations which result in a similar uniform sampling of the *uv*-space.

A perfect array with a compact full baseline distribution will have the properties that the baseline-distribution will be symmetric under 60-degree rotations, provided that the number of baselines is a multiple of 6; and its total baseline length will be the shortest for that number of unique baselines. The 7-element arrays with the most compact baseline distributions shown in Figure 2 are not perfect since both the symmetric and non-symmetric layouts result in baseline distributions with gaps inside the circle of maximum *uv*-distance. Thus, the 7-element array from the EISCAT design study (Grydeland & La Hoz, 2006, Figure 6) is not considered perfect as there are non-populated grid points on the *uv*-plane.

4. Discussion

A 2-D array conforming to a hexagonal grid is referred to as a honeycomb array (Blackburn, Panoui, et al., 2010). These perfect arrays, including the Manx array layout, are thus all honeycomb arrays. Investigation of arrays for numbers of elements greater than or equal to the Manx array, indicate there are no further perfect solutions. The hexagonal grid is the 2-D equivalent of close-cubic packing and represents the complete packing density of elements (Conway & Sloane, 1995).

The Manx array is consistent with the experiences from radio astronomy, where nominal module positions are sought along log-spiral arms. The baselines are equispaced with no redundancies or omissions (apart from the center "zero-spacing"). The 1-D case is the Golomb ruler, which is a set of specific integer positions along a line such that no two pairs of points are the same distance apart (Golomb & Taylor, 1984). This is specifically applicable to earth rotation aperture synthesis (Arsac (1955), cited in [Thompson et al., 2017]).

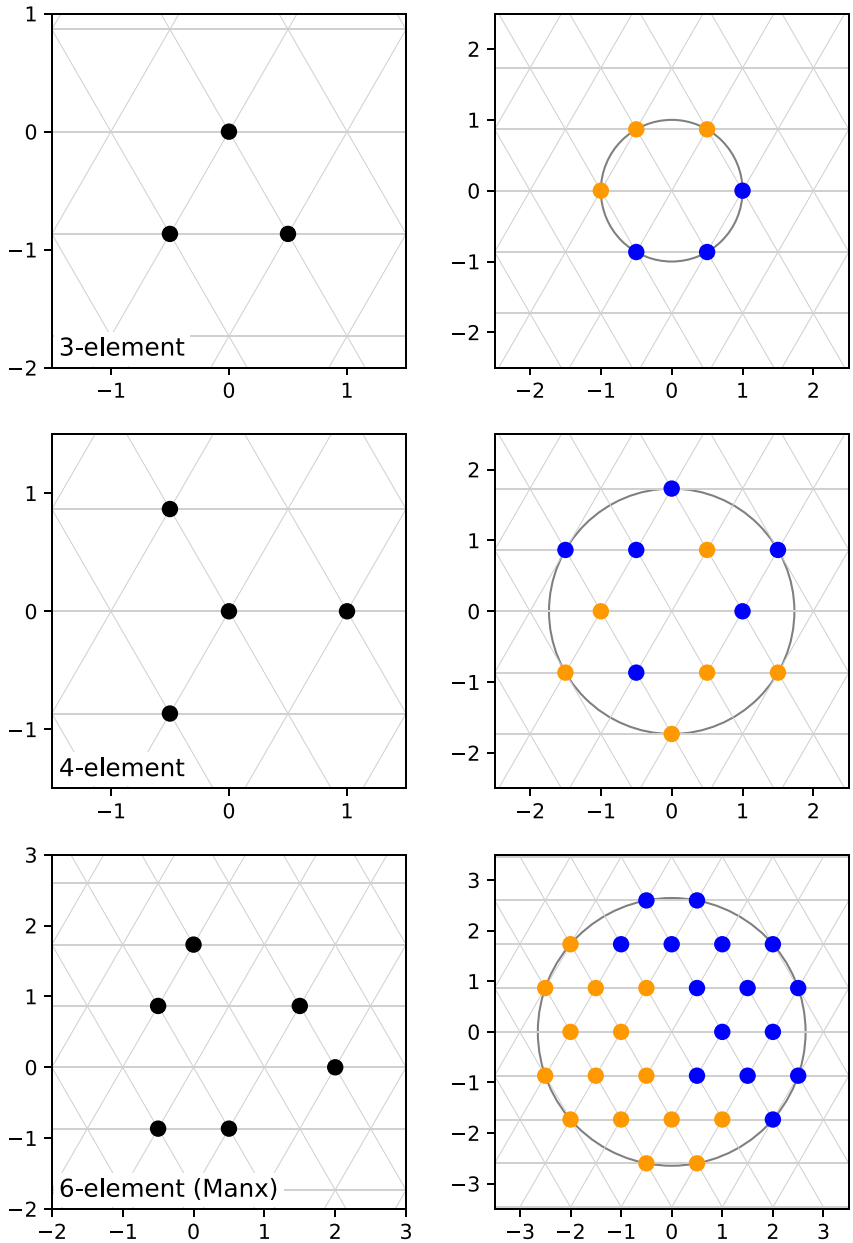

Figure 1. The set of perfect Golomb-Honeycomb arrays are plotted in the left panels, while the corresponding difference-vector distributions are shown in the right panels. The amber-blue colors show the conjugate pairs. The circles indicate the radius of maximum baseline. Note that the Manx array has a chiral opposite.

Studies have been carried out on 2-D patterns considering similar properties (e.g., Blackburn, Etzion, et al., 2010). The 2-D version of the Golomb ruler is the Costas array (Barker et al., 2009; Costas, 1984). These are orthogonal Cartesian arrangements, though some Costas arrays can be skewed into hexagonal honeycomb arrays (e.g., Blackburn, Panoui, et al., 2010; Golomb & Taylor, 1984). Such arrangements and their applications have been discussed in numerous publications (e.g., Luke, 1988; Nishimura & Sato, 2009; Robinson, 1985; Shearer, 1995). Kopilovich (1984) investigated both cartesian and hexagonal packings, but omitted the Manx array configuration.

The beam pattern intensity $I(l, m)$, for the array can be determined using a discrete Fourier transform (Thompson et al., 2017):

$$I(l,m) = \iint e^{2\pi i(ul+vm)}\,\mathrm{d}l\mathrm{d}m \tag{3}$$

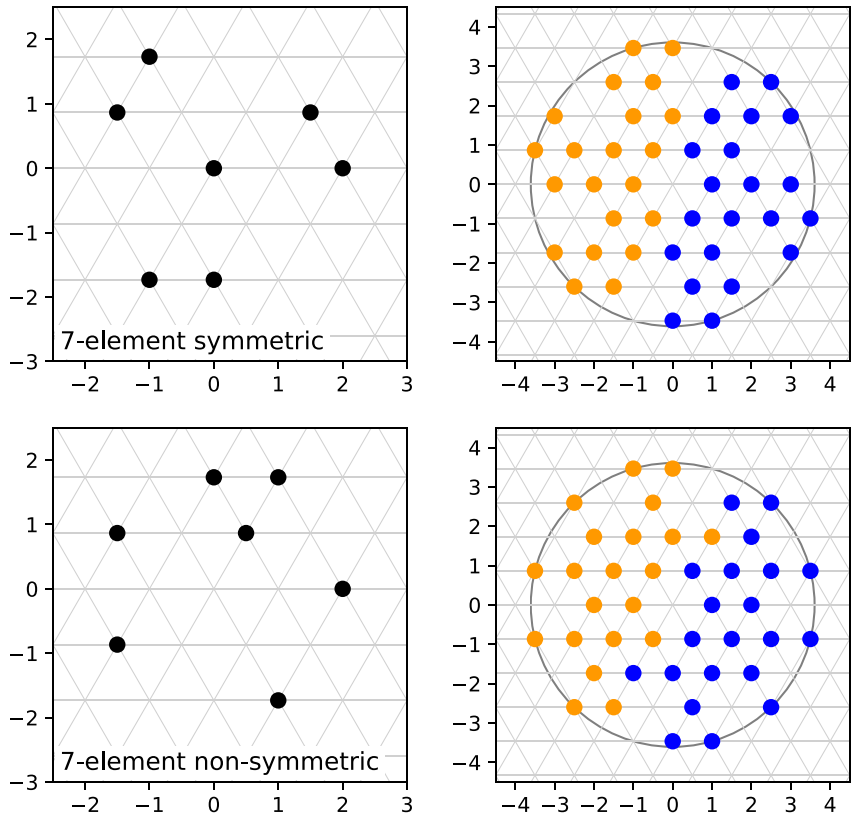

Figure 2. The "best" symmetric 7-element array (from figure 6 in Grydeland and La Hoz (2006)), presented in a similar manner to Figure 1 in the top row and the "best" in the bottom row. Unlike the perfect Golomb-Honeycomb arrays, these layouts have gaps inside the circle of maximum baseline-length. Similar to the Manx array, these 7-element arrays have chiral opposites.

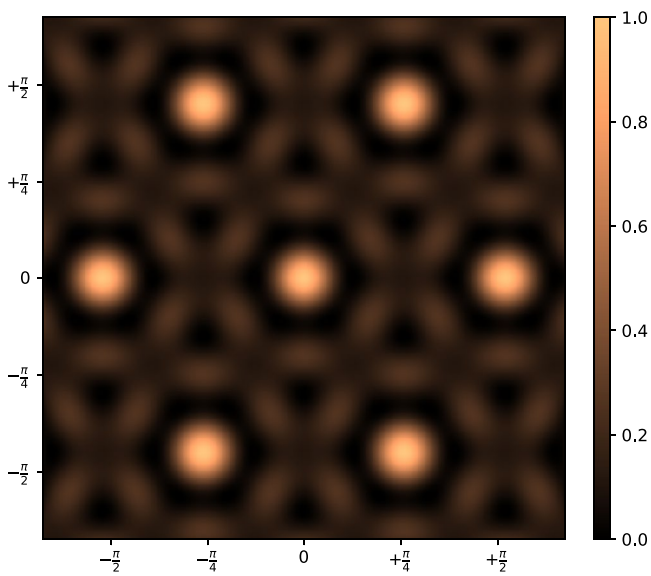

Figure 3. A 2-D discrete Fourier transform of the 6-element Manx array. The intensity scale is linear and is normalized to the central peak.

where u, v are the coordinates in the Fourier domain and l, m are the coordinates in the image domain (which is a plane normal to the boresight vector). This is shown in Figure 3, centered on the zeroth antinode and with the axes extended sufficiently to show the first antinodes. In practice these could be suppressed by the beam pattern of the individual antenna elements.

The Manx array has several significant implications. It represents an optimal arrangement for six elements, which results in the lowest local maxima (sidelobes) between the antinodes. It is therefore useful for sparse arrays, such as VLBI (Very Long Baseline Interferometry) and outliers to existing large arrays, for example, for systems such as LOFAR (van Haarlem,. et al., 2013) or EISCAT_3D (van Eyken et al., 2009).

Another interesting property of the Manx array is that it is possible to cascade it into a fractal Cantor-dust type configuration. It is created by taking the point at [0, 0] and replicating it at the Manx coordinates, m from Equation 2. Then for the next expansion, the next-level unit-vectors for the next larger triangular equilateral grid are calculated as:

$$\begin{aligned} \vec{e}_1^{\,i+1} &= 5\vec{e}_1^{\,i} + 1\vec{e}_2^{\,i} \\ \vec{e}_2^{\,i+1} &= -1\vec{e}_1^{\,i} + 6\vec{e}_2^{\,i} \end{aligned} \tag{4}$$

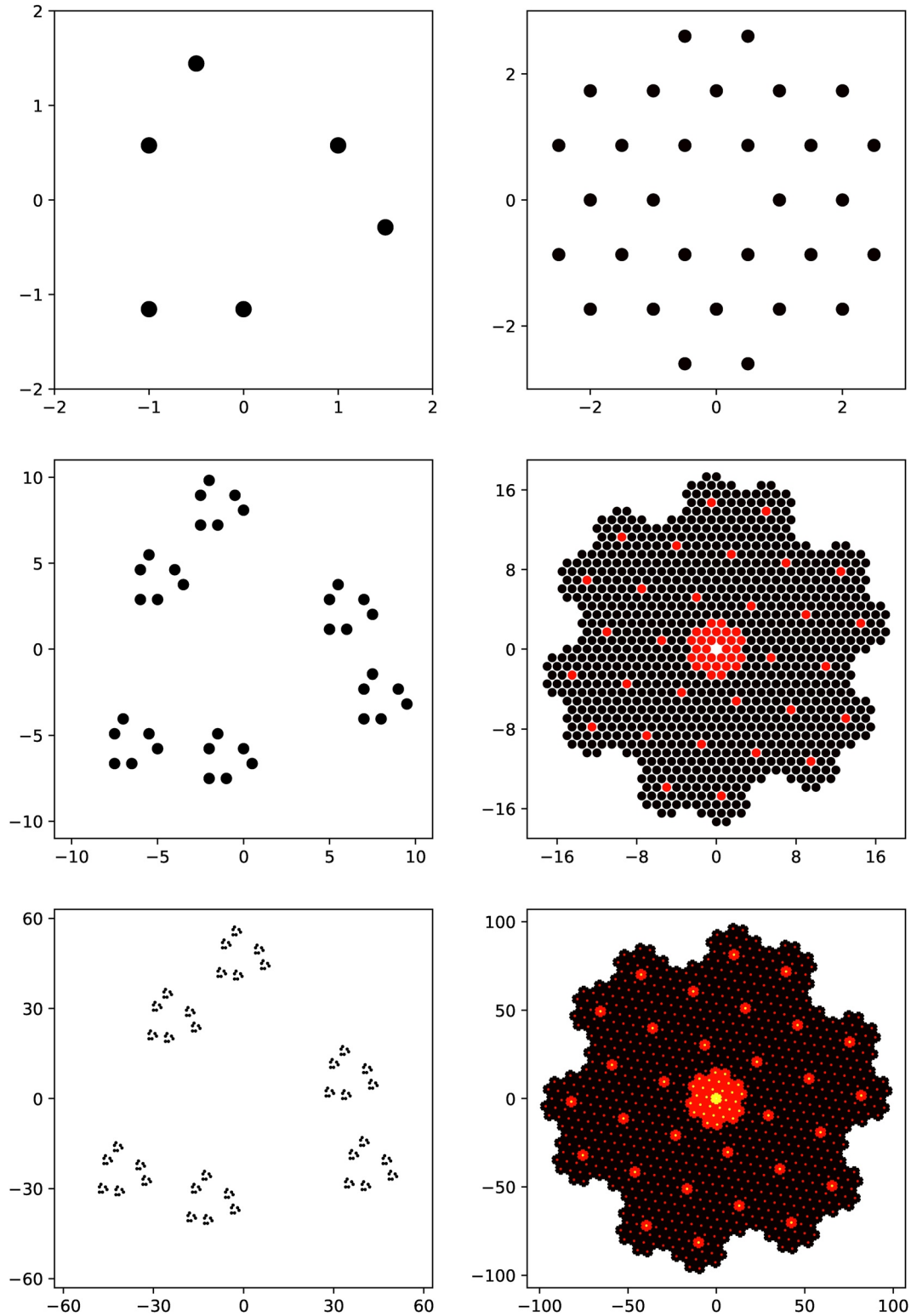

Figure 4. The Manx array layout (top left) and its *uv*-coverage (top right) are fractally expanded. The middle row is the configuration after the first expansion. This is repeated a second time for the layout/configuration in the third row. The colors in the *uv*-coverage plots shows the increase in the occurrence of redundant baselines, for no-redundancy (black), 6-fold redundancy (red) and 36-fold (yellow).

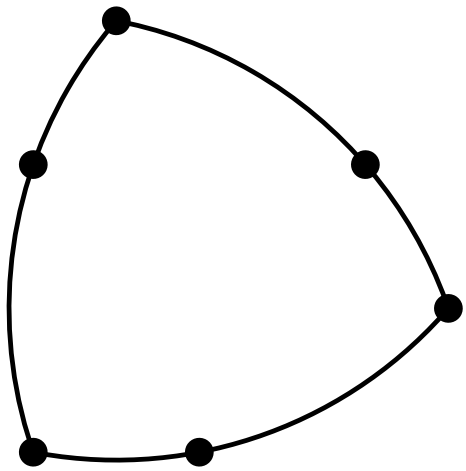

Figure 5. The nodes of the Manx array lie on the Reuleaux triangle of width $\sqrt{7}s$, where s is the separation between close nodes.

where $\vec{e}_1^{\,i}$ are unit vectors from Equation 1. For each iterative expansion, $i+1$, the Cantor-Manx array of the ith level are replicated and placed with the [0, 0] elements. Thus, new node vectors, r_n, are:

$$\begin{aligned}
\vec{r}_1 &= 0\vec{e}_1^{\,i+1} + 0\vec{e}_2^{\,i+1} \\
\vec{r}_2 &= 1\vec{e}_1^{\,i+1} + 0\vec{e}_2^{\,i+1} \\
\vec{r}_3 &= 2\vec{e}_1^{\,i+1} + 1\vec{e}_2^{\,i+1} \\
\vec{r}_4 &= 1\vec{e}_1^{\,i+1} + 2\vec{e}_2^{\,i+1} \\
\vec{r}_5 &= -1\vec{e}_1^{\,i+1} + 2\vec{e}_2^{\,i+1} \\
\vec{r}_6 &= -1\vec{e}_1^{\,i+1} + 3\vec{e}_2^{\,i+1}
\end{aligned} \tag{5}$$

Each subsequent Cantor-Manx configuration will be scaled by a factor of $\sqrt{31}$ and will be rotated by $\tan^{-1}(5 + \cos(\pi/3)/\sin(\pi/3))$. As all elements fall on the lattice-points, the baseline distribution will remain compact, and the baselines will have repeated u, v samples at tiered regular spacings, where there will be a compact region at short baseline lengths and a regular sparse sampling at longer baselines. The first three Cantor-Manx-arrays are shown in Figure 4, where the antenna locations are on the left-hand graphs, and the uv-coverage is on the corresponding right-hand side panel.

It is claimed that interferometer configurations based on slightly perturbed curves of constant width, in particular the Reuleaux triangle, offer the most complete sampling in the Fourier space of the image (Keto, 1997). This is asserted not only for instantaneous beam forming in which the spectral response is the cross-correlation function of the antenna locations at a given instant, but is also applicable in Earth rotation synthesis in which the response is a time integration of the changing instantaneous responses obtained in tracking a source from rise to set across the sky (Keto, 1997). For imaging off boresight a foreshortening of the beam is expected, as per any 2-dimensional planar array. The Manx array lies on a Reuleaux triangle as shown in Figure 5.

5. Conclusion

The Manx array represents the configuration of the largest number (= 6) of interferometric elements such that the distribution of element spacings is uniform and complete within a circle of radius equal to the maximum uv-distance. It has the property that it contains no redundant baselines. It is elegant and provides a practical layout for small array configurations.

Data Availability Statement

This paper is a theoretical presentation. Data were not used, nor created for this research.

Acknowledgments
The work by D. McKay is partly supported by the Academy of Finland, Finland (project no.322535). The authors thank the two anonymous reviewers for their feedback and constructive criticism which helped improve this work.

References

Arsac, J. (1955). Transmissions des fréquences spatiales dans les systèmes récepteurs d'ondes courtes. *Optica Acta: International Journal of Optics*, *2*(3), 112–118. https://doi.org/10.1080/713821025

Barker, L., Drakakis, K., & Rickard, S. (2009). On the complexity of the verification of the Costas property. *Proceedings of the IEEE*, *97*(3), 586–593. https://doi.org/10.1109/JPROC.2008.2011947

Blackburn, S. R., Etzion, T., Martin, K. M., & Paterson, M. B. (2010). Two-dimensional patterns with distinct differences—Constructions, bounds, and maximal anticodes. *IEEE Transactions on Information Theory*, *56*(3), 1216–1229. https://doi.org/10.1109/TIT.2009.2039046

Blackburn, S. R., Panoui, A., Paterson, M. B., & Stinson, D. R. (2010). Honeycomb arrays. *Electronic Journal of Combinatorics*, *17*(R172), 1. https://doi.org/10.37236/444

Boone, F. (2001). Interferometric array design: Optimizing the locations of the antenna pads. *Astronomy & Astrophysics*, *377*(1), 368–376. https://doi.org/10.1051/0004-6361:20011105

Boone, F. (2002). Interferometric array design: Distributions of Fourier samples for imaging. *Astronomy & Astrophysics*, *386*(3), 1160–1171. https://doi.org/10.1051/0004-6361:20020297

Cohanim, B. E., Hewitt, J. N., & de Weck, O. (2004). The design of radio telescope array configurations using multiobjective optimization: Imaging performance versus cable length. *The Astrophysical Journal Supplement Series,* *154*(2), 705–719. https://doi.org/10.1086/422356

Conway, J. H., & Sloane, N. J. A. (1995). What are all the best sphere packings in low dimensions? *Discrete & Computational Geometry*, *13*(3–4), 383–403. https://doi.org/10.1007/BF02574051

Cornwell, T. J. (1988). A novel principle for optimization of the instantaneous Fourier plane coverage of correlation arrays. *IEEE Transactions on Antennas and Propagation*, *36*(8), 1165–1167. https://doi.org/10.1109/8.7233

Costas, J. P. (1984). A study of a class of detection waveforms having nearly ideal range—Doppler ambiguity properties. *Proceedings of the IEEE*, *72*(8), 996–1009. https://doi.org/10.1109/PROC.1984.12967

De Villiers, M. (2007). Interferometric array layout design by tomographic projection. *Astronomy and Astrophysics*, *469*(2), 793–798. https://doi.org/10.1051/0004-6361:20077351

Gauci, A., Zarb Adami, K., Abela, J., & Cohanim, B. E. (2013). Genetic optimization for radio interferometer configurations. *Monthly Notices of the RAS*, *431*(1), 322–326. https://doi.org/10.1093/mnras/stt163

Golomb, S., & Taylor, H. (1984). Constructions and properties of Costas arrays. *Proceedings of the IEEE*, *72*(9), 1143–1163. https://doi.org/10.1109/PROC.1984.12994

Greenaway, H. A. (1979). The interferometric observing efficiency of arrays of large aperture telescopes. *Optics Communications*, *29*(3), 279–283. https://doi.org/10.1016/0030-4018(79)90099-3

Greenbaum, A. Z., Pueyo, L., Sivaramakrishnan, A., & Lacour, S. (2014). An image-plane algorithm for JWST's non-redundant aperture mask data. *The Astrophysical Journal*, *798*(2), 68. https://doi.org/10.1088/0004-637X/798/2/68

Grydeland, T., Chau, J. L., La Hoz, C., & Brekke, A. (2005). An imaging interferometry capability for the EISCAT Svalbard Radar. *Annales Geophysicae*, *23*(1), 221–230. https://doi.org/10.5194/angeo-23-221-2005

Grydeland, T., & La Hoz, C. (2006). D5.1 EISCAT_3D radar imaging arrays configurations report. *EISCAT 3D Design Study*.

Hogbom, J. A., & Brouw, W. N. (1974). The synthesis radio telescope at Westerbork. Principles of operation, performance and data reduction. *Astronomy & Astrophysics*, *33*, 289.

Huang, S., Guo, Y., & Rao, C. (2019). Non-redundant array configurations for optical interferometric systems combined with a large telescope. *Optik*, *178*, 343–350. https://doi.org/10.1016/j.ijleo.2018.10.040

Karastergiou, A., Neri, R., & Gurwell, M. A. (2006). Adapting and expanding interferometric arrays. *The Astrophysical Journal Supplement Series*, *164*(2), 552–558. https://doi.org/10.1086/503630

Keto, E. (1997). The shapes of cross-correlation interferometers. *The Astrophysical Journal*, *475*(2), 843–852. https://doi.org/10.1086/303545

Kiehbadroudinezhad, S., Valente, D., Cada, M., Kamariah Noordin, N., & Shahabi, A. (2017). Optimization of positioning of interferometric array antennas using division algorithm for radio astronomy applications. *The Astronomical Journal*, *154*(4), 167. https://doi.org/10.3847/1538-3881/aa8ad3

Kogan, L. (2000). Optimizing a large array configuration to minimize the sidelobes. *IEEE Transactions on Antennas and Propagation*, *48*(7), 1075–1078. https://doi.org/10.1109/8.876326

Kopilovich, L. (1984). Non-redundant aperture mask systems for interferometric image synthesis. *Optica Acta: International Journal of Optics*, *31*(12), 1409–1415. https://doi.org/10.1080/713821465

Kopilovich, L. (1998). Non-redundant apertures for optical interferometric systems: Maximization of the number of elements. *Journal of Modern Optics*, *45*(11), 2417–2424. https://doi.org/10.1080/09500349808231250

Luke, H. D. (1988). Sequences and arrays with perfect periodic correlation. *IEEE Transactions on Aerospace and Electronic Systems*, *24*(3), 287–294. https://doi.org/10.1109/7.192096

McKay-Bukowski, D., Vierinen, J., Virtanen, I. I., Fallows, R., Postila, M., Ulich, T., et al. (2015). KAIRA: The Kilpisjärvi atmospheric imaging receiver array—System overview and first results. *IEEE Transactions on Geoscience and Remote Sensing*, *53*(3), 1440–1451. https://doi.org/10.1109/TGRS.2014.2342252

Nishimura, K., & Sato, T. (2009). Two-dimensional arrays optimized for wide-scanning phased array based on potential function method. *IEICE—Transactions on Communications*, *92*(10), 3228–3235. https://doi.org/10.1587/transcom.E92.B.3228

Robinson, J. (1985). Golomb rectangles. *IEEE Transactions on Information Theory*, *31*(6), 781–787. https://doi.org/10.1109/TIT.1985.1057108

Sallum, S., & Skemer, A. (2019). Comparing non redundant masking and filled-aperture kernel phase for exoplanet detection and characterization. *Journal of Astronomical Telescopes, Instruments, and Systems*, *5*(1), 018001. https://doi.org/10.1117/1.JATIS.5.1.018001

Shearer, J. B. (1995). Some new optimum Golomb rectangles. *Electronic Journal of Combinatorics*, *2*(1), 12. https://doi.org/10.37236/1206

Su, Y., Nan, R., Peng, B., Roddis, N., & Zhou, J. (2004). Optimization of interferometric array configurations by "sieving" u–v points. *Astronomy & Astrophysics*, *414*(1), 389–397. https://doi.org/10.1051/0004-6361:20031607

Taylor, G. B., Carilli, C. L., & Perley, R. A. (1999). Synthesis imaging in radio astronomy II (Vol. *180*).

Thompson, A. R., Moran, J. M., & Swenson, G. W. (2017). Antennas and arrays. In *Interferometry and synthesis in radio astronomy* (pp. 153–206). Springer International Publishing. https://doi.org/10.1007/978-3-319-44431-4_5

van Eyken, T., Turunen, E., Wannberg, G., Andersson, H., Behlke, R., Belyey, V., et al. (2009). *EISCAT_3D final design study report, deliverable D11.1*, In D. McKay & I. McCrea (Eds.) (Vol. D11.1). EISCAT Scientific Association. Retrieved from https://cloud.eiscat.se/index.php/s/XH2Y3mQeXat5wdW?dir=undefined%26path=/Reports%26openfile=19255

van Haarlem, M. P., Wise, M. W., Gunst, A. W., Heald, G., McKean, J. P., Hessels, J. W. T., et al. (2013). LOFAR: The LOw-Frequency ARray. *Astronomy & Astrophysics*, *556*. https://doi.org/10.1051/0004-6361/201220873